Experimental and Computational Analysis of a Rotating Detonation Combustor

Jonathan R. Tobias[1] and Ajay K. Agrawal[2]
Department of Mechanical Engineering, University of Alabama Tuscaloosa, Alabama, 35401

Daniel E. Paxson[3]
NASA Glenn Research Center, Cleveland, Ohio, 44130

Rotating detonation combustor (RDC) research has progressed along parallel experimental and computational paths with limited opportunities for validation. Validation is a crucial step to ensure RDC simulations provide an accurate representation of the physical phenomena, and thus, can be used with confidence for design optimization in different applications. In this study, data from a quasi-two-dimensional computational fluid dynamic simulation in an annular RDC are compared with experimental measurements including particle image velocimetry at 100 kHz. Results show good agreement between measured and simulated dynamic pressures, Chapman-Jouguet speeds, and static pressure distributions. Velocity measurements at the annulus exit show good temporal and quantitative agreement with simulations including spikes from the passing shock.

I. Nomenclature

p	=	pressure
p_{man}	=	manifold pressure
u	=	azimuthal (circumferential) velocity
u_{det}	=	detonation speed
v	=	axial velocity
x	=	non-dimensional circumferential direction
y	=	non-dimensional axial direction
z	=	axial location [mm]
ρ	=	density
ε	=	ratio of orifice flow area to RDC annulus area

II. Introduction

Pressure gain combustion (PGC) has gained attention for its potential to increase fuel efficiency by converting a portion of the chemical energy of the fuel directly into work, for example, by a detonation combustion process, and thus reducing the entropy production[1-3]. Replacing deflagration combustion with detonation combustion in constant pressure, continuous flow systems such as gas turbines is currently under extensive study[4]. Rotating detonation combustion (RDC) uses a circular track to continuously rotate the detonation wave so long as the conditions remain favorable for detonation[5-6]. Studies of RDC are increasingly focused on optical diagnostics to acquire quantifiable data

---

[1] Graduate Researcher, Mechanical Engineering, AIAA Student Member
[2] Robert F. Barfield Endowed Chair Professor, Mechanical Engineering, aagrawal@eng.ua.edu, AIAA Associate Fellow.
[3] Aerospace Research Engineer, Research and Engineering Directorate, 21000 Brookpark Road/MS 77-1, AIAA Associate Fellow

of the detonation wave and the flow field to develop practical designs[7-10]. Detonation within the annulus has been optically studied using OH* chemiluminescence by Rankin et al.[11]. RDC exhaust flow has been investigated using OH* chemiluminescence by Tobias et al.[12] and Rainbow Schlieren Deflectometry (RSD) by Miller et al[13].

RDC technology has shown potential for a variety of applications for propulsion and power generation. While the fundamental operation of the RDC remains similar, the requirements for optimization of the flow field – downstream of the annulus – are unique to each application. Thus, flow field characterization downstream of the detonation zone is paramount for successful system integration. Computational efforts typically focus on analysis within the annulus where boundary conditions are imposed downstream of the annulus exit. Simulations of RDCs also tend to vary greatly in complexity across the research field. Experimental efforts are often limited in diagnostic options for annular flow analysis because of the harsh operating environment and inability for appropriate optical access in many RDC test rigs. Because of these limitations, experiments involving optical diagnostics such as particle image velocimetry (PIV) have been limited mainly to the exhaust flow field characterization. While this is advantageous for system integration, it does not present the details of the flow behavior in the region upstream of the exit nozzle, i.e., nozzle throat.

The throat of the RDC annulus offers a mid-plane between internal and external RDC flows to facilitate an easier comparison of computational and experimental results. In this study simulations using a computational algorithm developed at NASA Glenn Research Center are compared with time-resolved PIV measurements at 100 kHz acquired near the RDC exit plane at the University of Alabama (UA) RDC facility. Measurements and computations of dynamic and static pressure inside the annulus are also compared at multiple reactant flow rates to demonstrate the fidelity of the simulations to replicate the experimental results.

III. Experimental Setup

A schematic diagram of the RDC used in experimentation at UA is presented in Fig. 1a. The combustor utilizes three concentric stacked rings (spools) and a circular center-body extending beyond the annulus exit as an aerospike. In this study, a conical shaped aerospike with 137.4 mm height and half-angle of 15° is used. The inner diameter of the annulus is 8.0 cm and the annular channel width is 1.0 cm. Figure 1a also shows the locations of static pressure capillary tube averaged pressure (CTAP) probes to measure the chamber pressure. The CTAP probes in this experiment consist of a static pressure transducer mounted at the end of a 3.175 mm (0.125 in.) diameter tube, one meter in length. This tube is attached to an opening on the annulus outer wall. The CTAP concept, introduced by Paxson et al.[14], attenuates pressure fluctuations to measure the time-averaged static pressure. The concept is useful
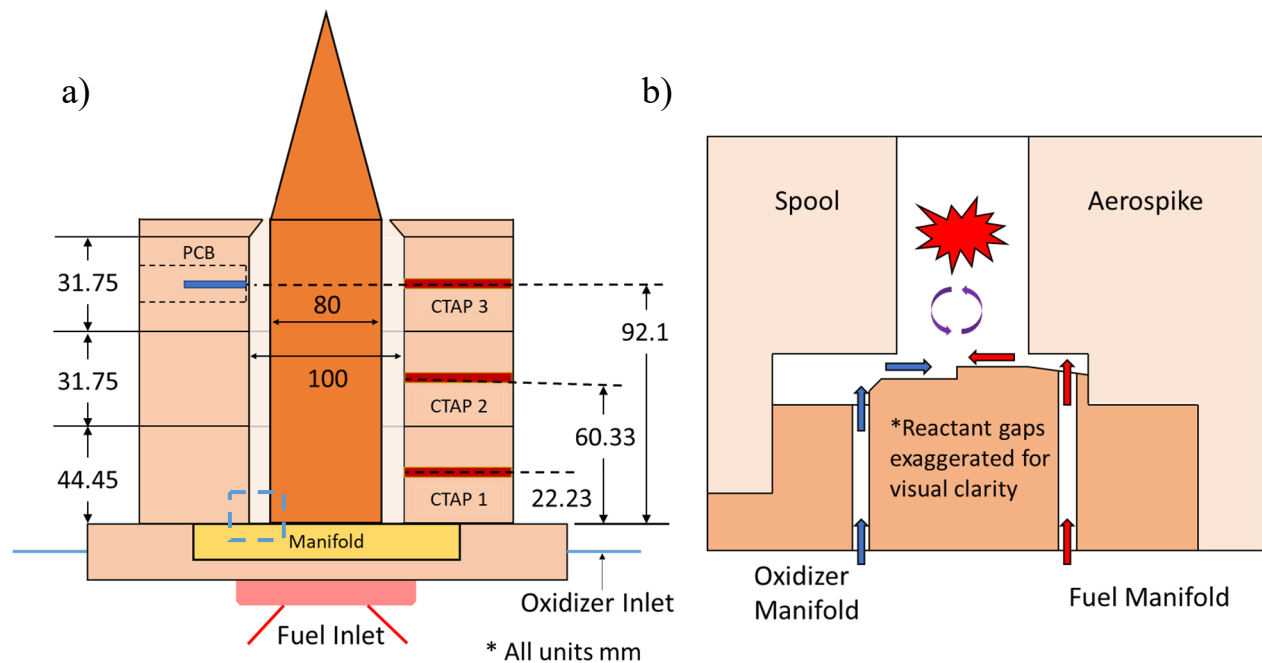

Fig. 1 (a) Schematic diagram of RDC geometry, (b) schematic diagram of injector geometry of the experiment RDC geometry.

since the total pressure in the annulus cannot be measured directly. Time resolved dynamic pressure fluctuations are measured by a charge-type probe (PCB 113B03). Together, the time-averaged static and time-resolved dynamic pressures provide an assessment of the total pressure behavior. A back-pressure plate (BPP) spool fitted with a converging nozzle with a contraction ratio of 1.7 is attached downstream of the third spool to elevate the operating pressure of the RDC.

The RDC is operated using methane fuel and oxygen-enriched air. Mass flow rate of each reactant gas supply system (methane, air, and oxygen) is controlled via sonic nozzles with critical flow venturis instrumented with pressure and temperature transducers. Figure 1b shows a cutaway schematic of the injection scheme. Reactants are injected through slots and mix at the base of the annulus. Inner and outer slots for fuel and air are configured such that opposing radial flow jets perpendicular to the annulus axis create turbulent mixing of gaseous reactants.

The experiment is controlled by an in-house developed system using BeagleBone microprocessors to precisely time the reactant flows and the ignition in the RDC. Further details of the test facility, instrumentation, and operation are given by Tobias et al.[12] and Welch et al.[15]. The PIV system uses a dual-head Photonics 100 W, 532 nm Nd-YAG laser. The laser pulse duration measured with a photodiode is 15 ns. The time between two consecutive laser pulses was measured to be 400 ns. The laser sheet was generated using a Galilean collimator resulting in a sheet thickness of approximately 1 mm at the annulus exit. A Photron SA-5 Fastcam high-speed digital CMOS camera with a Sigma 105 mm focal length lens was used to acquire the PIV images. A 532 nm band-pass optical filter is mounted on the camera lens to isolate the laser light scattered by the seed particles. The seeded air flow is introduced into the main oxidizer flow upstream of the oxidizer manifold inlet with seed flow initiated prior to the ignition event. ZrO_2 seed of 200 nm diameter was used for this study. Further details of the fluidized bed seeder can be found in Depperschmidt et al.[16]. Each individual laser head operated at 100 kHz, the camera operated at 200 kHz, to yield velocity data at 100 kHz or at 10 µs timesteps. TSI Insight 4G Data Acquisition, Analysis, and Display software was used to acquire and process the PIV images.

Table 1 presents the operational parameters for a high-flowrate Case A, and a low-flowrate Case B. The heat release rate for Case A at equivalence ratio of 1.00 was calculated as 3.63 MW. Case A had an operational frequency of 6.4 kHz. Similarly, the heat release rate for Case B at equivalence ratio of 0.98 was calculated as 2.27 MW. Case B had an operational frequency of 5.8 kHz. Both operational frequencies indicate a single rotating detonation wave in the annulus.

Table 1. Experimental Test Conditions

		Case A	Case B
Enthalpy of Reaction	[MW]	3.63	2.27
Equivalence Ratio	[ϕ]	1.00	0.98
Methane mass flowrate	[kg/s]	0.073	0.045
Oxygen mass flowrate	[kg/s]	0.254	0.160
Primary air mass flowrate	[kg/s]	0.161	0.098

IV. Numerical Approach

The simulation procedure used in this paper has been detailed in the literature and will only be briefly described here[17-20]. The basis is a high resolution, computational fluid dynamic (CFD) algorithm that integrates the quasi-two-dimensional (Q2D), single-species, reactive Euler equations with source terms. The CFD code adopts the detonation frame of reference and deliberately utilizes a course grid (i.e., it is diffusive) to eliminate the highest frequency unsteadiness (e.g., detonation cells, Kelvin-Helmholtz phenomena). The result is a flow field solution that is invariant with time when converged. The working fluid is assumed to be a single, calorically perfect, premixed gas. The source terms contain sub-models which govern the reaction rate, momentum losses due to skin-friction, and the effects of heat transfer to the walls. The sub-models are adapted from validated one-dimensional sub-models used to investigate pulse detonation engines and other gas dynamic devices[21-23].

The governing equations are integrated numerically in time using an explicit, second-order, two-step, Runge-Kutta technique. Spatial flux derivatives are approximated as flux differences, with the fluxes at the discrete cell faces evaluated using Roe's approximate Riemann solver. Second-order spatial accuracy (away from discontinuities) is

obtained using piecewise linear representation of the primitive variable states within the cells (MUSCL). Oscillatory behavior is avoided by limiting the linear slopes.

Considering an 'unwrapped' RDC where the non-dimensional circumferential direction is x, and the axial direction is y, the following boundary conditions are imposed. At x=0.0 and x=1.0, periodic (aka symmetric) conditions are used. These conditions ensure that the x-dimension of the computational space faithfully represents an annulus (which is continuous and has no boundary). At y=y_{max}, constant pressure outflow is imposed along with characteristic equations to obtain density, ρ, and axial velocity, v for the image cells. If the resulting flow is sonic, or supersonic, then the imposed pressure is disregarded. If, in addition, the upstream flow is supersonic, then pressure, p, ρ, and v are extrapolated from the interior[24]. The possibility for a normal shock solution whereby supersonic outflow jumps to subsonic is also accommodated. The x-velocity (azimuthal) component u is extrapolated from the interior at each boundary location. At y=0.0 (the inflow face), partially open boundary conditions are applied as described and validated in Ref. 25. This face is presumably fed by a large manifold at a fixed total pressure, and temperature. The manifold terminates at the face and is separated from it via an orifice. The ratio of orifice flow area to RDC annulus area, ε is generally less than 1. If the interior pressure is less than the manifold pressure, p_{man}, then inflow occurs. The boundary condition routine determines p, ρ, and v for the inflow face image cells subject to a momentum (total pressure) loss model which depends on the mass flow rate and the value of ε. It is capable of accommodating a scenario where the orifice becomes choked. The x-velocity component u is prescribed during inflow, and it is here that a reference frame change is implemented. Rather than specify u=0 (i.e., no swirl) which is the laboratory or fixed frame condition, the negative of the detonation speed, u_{det} is prescribed instead. As a result of this change to the detonation reference frame, the computational space becomes one where a steady-state solution is possible.

If the interior pressure along the inlet face is greater than p_{man}, as might be found just behind the detonation, then there will be backflow into the manifold through the orifice. The boundary condition routine can accommodate this as well. In RDC simulations where inlet backflow occurs, the total mass and enthalpy of backward flow are averaged over the circumferential backflow span (recalling that in the steady detonation frame of reference, time is simply span divided by detonation velocity). When the interior pressure subsequently drops below p_{man} and forward flow resumes, all of the mass that flowed backward is sent back into the RDC at the same average enthalpy that it exited. Once this mass has re-entered, the prescribed manifold premixed air and fuel mixture enthalpy is used.

Although the model assumes that premixed air and fuel enter through the inlet, the reality of most RDC experiments is that fuel and air are injected separately. The dynamics and feed pressures of the two injection systems can be quite different, particularly during lean operation. This raises the possibility that as the rotating detonation passes a given point, it may stop or even reverse the flow in both injectors; however, the resumption of inflow may occur at different times in each. This, in turn, may raise the possibility of a purging period where air enters the RDC for part of the cycle without having fuel added to it. To crudely explore the effects of this possibility, the prescribed inlet reactant fraction of the model may be set to zero over various portions of the circumference.

Another real-world effect of separate fuel and air injection is the possibility that some finite time (and associated convection distance) is required to mix before they will react. To cursorily examine the effect of this reaction delay, the simulation allows a user specified number of axial computational cell rows near the inlet that do not react, even though the threshold temperature is reached. The experiment simulated here has a very small value of ε, and correspondingly high manifold pressures. As such, it is not expected to exhibit the injector dynamics just described. An investigation of purge effects was not undertaken. A brief study of mixing delay effects was made and the limited data available (PCB, and CTAP measurements) did not indicate that this was occurring. The best match to the data occurred when no delay was assumed.

A Q2D code cannot duplicate the rapid cross-sectional area contraction associated with the experimental exit throat region. As such, a smooth and more gradual contraction profile was used which starts at an axial distance of 97 mm and ends at the RDC exit. The code exit area is 10% less than that of the experiment to account for the poor aerodynamics associated with the rapid contraction. The manifold pressure of the code was set to match that of the experiment. The code inlet area was adjusted until the computed mass flow matched the measured mass flow rate of propellants to within 1%. The required area was just 7% greater than the measured area of the combined experimental fuel and air inlets.

V. Results

Case A: Dynamic & Static Pressure Comparison

Figure 2 shows the experimental time-history of pressure in the fuel and oxidizer manifolds, upstream of the injection point, for Case A. The fuel manifold pressure is steady at around 1,025 kPa. The oxidizer manifold shows

an initial attempted stabilization between 1,050-1,100 kPa. After 100 ms the oxidizer manifold pressure increases to 1,150 kPa before stabilizing at an average pressure of about 1,120 kPa for the rest of the test duration.
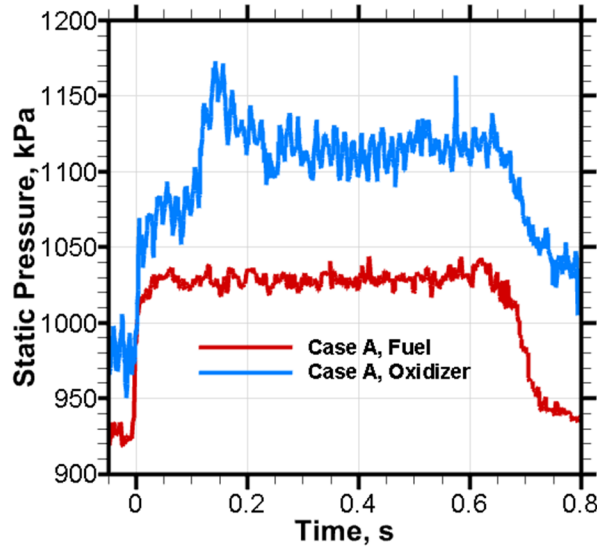

Fig. 2 Fuel and oxidizer manifold pressure history for experiment, Case A (high flowrate).

The dynamic pressure is measured at the outer wall of the annulus at, $z = 92$ mm, the distance downstream of the point of injection. The dynamic pressure data from the experiment in Fig. 3, shown in blue for 3 consecutive cycles, reveals a double peak behavior. This double peak appears to be phase locked throughout the test duration which suggests that the secondary peak is a shock reflection trailing the initial shock from the detonation. The experimental measurements show the initial peak at a lower pressure than the secondary peak for each cycle. This is likely due to the mounting scheme of the piezoelectric pressure transducer. The face of the probe is mounted in a jacket with a 3.8 mm long and 2 mm diameter recessed cavity to protect the sensing element from the extreme temperatures within the annulus. Thus, the impulse of the passing shock is likely attenuated by the cavity. The subsequent reflected shockwave from the exit is captured at a relatively elevated pressure compared to the initial shock wave because the impulse of the reflected shock occurs over a longer duration; attenuation effects are thus relatively less pronounced. Further assessment of the effect of recessing the dynamic pressure probe in the RDC will confirm or negate this explanation.

Simulated dynamic pressure is presented in magenta in Fig. 3. The computed dynamic pressure shows a very good agreement with experimental results. The shock front and reflection are both visible. The primary peak has a 40 kPa higher pressure compared to the secondary peak in the simulation. While the difference is marginal, this suggests
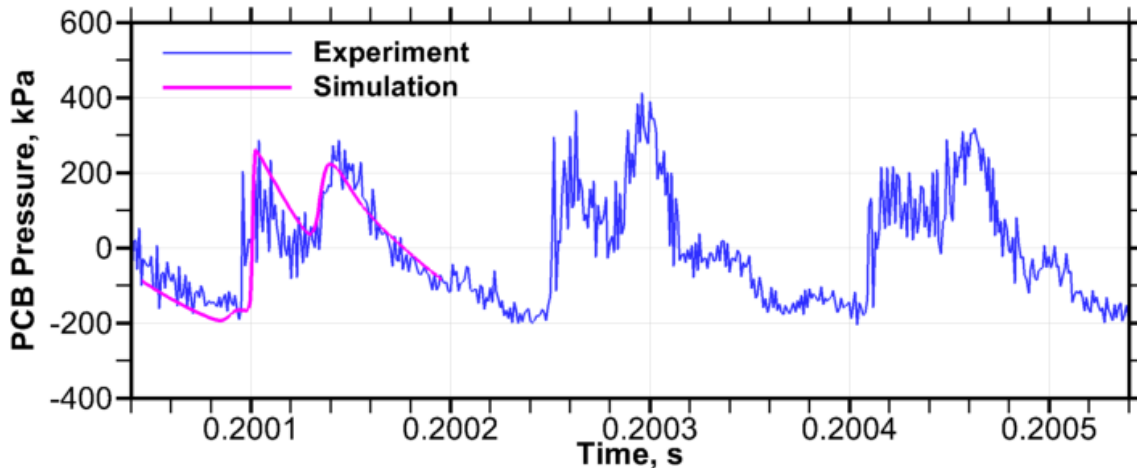

Fig. 3 Comparison of measured and simulated dynamic pressure for Case A, inside the RDC annulus at $z = 92.0$ mm.

5

that the measured dynamic pressure is realistic, adding that the attenuation effects of the recessed probe could affect accuracy at only the smallest time scales within the annulus. The measured pressure for the secondary peak is expected to be marginally higher that the model. The peak-to-peak time between the computed and measured values is approximately the same with the code predicting a 6.6 kHz operation, while the measurements show 6.4 kHz wave frequency, about 83% of the C-J speed. The agreement in both dynamic pressure and wave frequency is an encouraging result.

Fig. 4a presents static pressure measurements for Case A. The upstream CTAP 1 near the detonation region (z=22.3 mm) shows an average pressure of 425 kPa. The downstream CTAP 3 at z=92 mm reaches a steady-state pressure of 380 kPa in 50 ms after the test begins. The pressure at the downstream location is unaffected by the transient phenomenon upstream in the detonation zone. Fig. 4b compares an axial profile of simulated time-averaged static pressure along the annulus with the steady-state CTAP 1 and CTAP 3 measurements. The simulation calculates 400 kPa at the CTAP 1 location, a 6% difference from the CTAP 1 steady-state pressure of 425 kPa. Both the computed and measured pressures at the CTAP 3 location are 380 kPa. Computed time-averaged static pressure is again in good agreement with the measured CTAP values.

The profile shape of the time-averaged static pressure from the simulation takes on a noticeable non-linear distribution from the injection location to RDC exit. At, z=1 mm, the static pressure is 490 kPa signifying a high-pressure detonation zone with a low-pressure refill region. The pressure decreases to 340 kPa by z=15 mm, before increasing back to 410 kPa at z=30 mm. This axial region represents the end of the detonation front and the beginning of the oblique shock front. The decrease in time-averaged pressure axially correlates with the area of flow axially above the extreme pressures of the detonation zone, but below the expansion zone from the shockwave. The profile shows decreasing pressure along most of the annulus until a trough of 360 kPa is reached at z=75 mm. Pressure increases again to 408 kPa until, z=100 mm, likely due to the higher strength of the reflected shock in this region. The location, z=100 mm, corresponds to the beginning of the nozzle geometry in the simulation and thus pressure decreases to 277 kPa at the exit, z=114 mm as the flow accelerates towards the nozzle throat.

Figure 5 illustrates the contour plot of the simulated pressure on the 'unwrapped' RDC. Because the simulation operates in the detonation frame of reference this figure represents a fixed time. If converted back to the laboratory frame of reference, the x-axis of the plot is analogous of time through repeatable cycles. The detonation wave is located near x=0.2 and extends to y=0.05, seen as the highest pressures in dark red. An oblique-shock is attached above the detonation zone where light blue meets the yellow – clearly denoting a sharp pressure gradient. This shock extends axially to the nozzle where the shock reflection is formed and the reflected shock travels back upstream in the annulus.
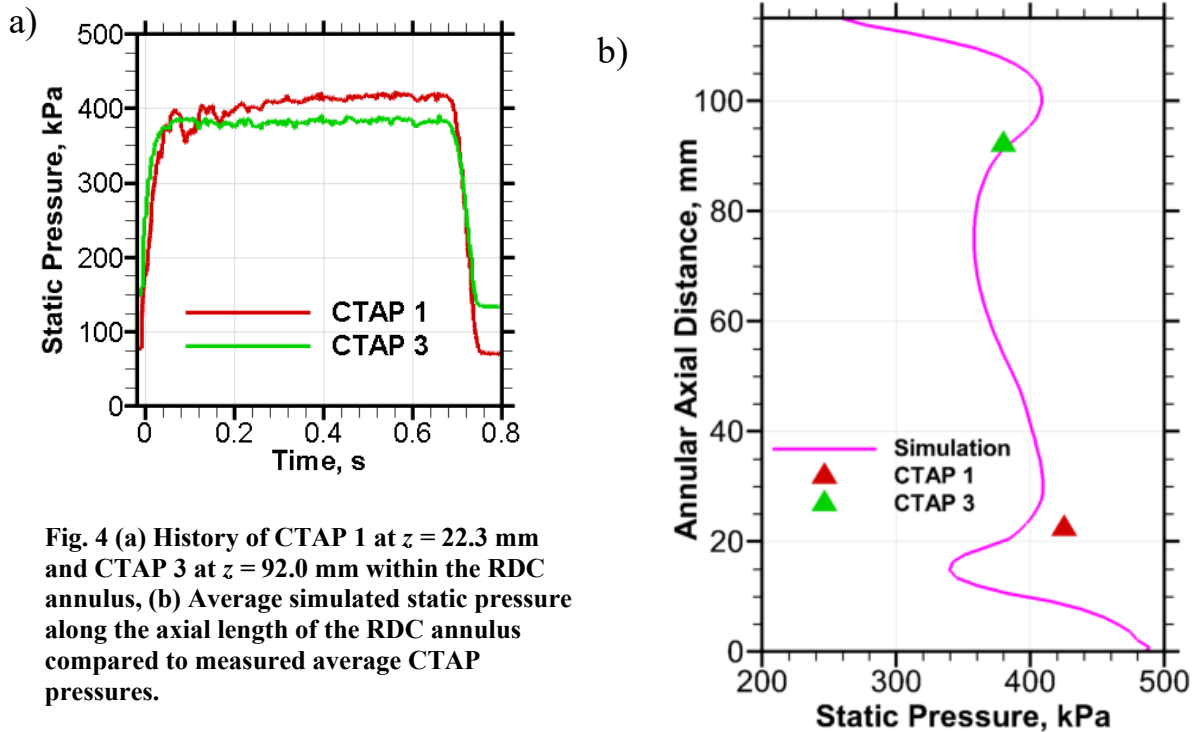

Fig. 4 (a) History of CTAP 1 at z = 22.3 mm and CTAP 3 at z = 92.0 mm within the RDC annulus, (b) Average simulated static pressure along the axial length of the RDC annulus compared to measured average CTAP pressures.
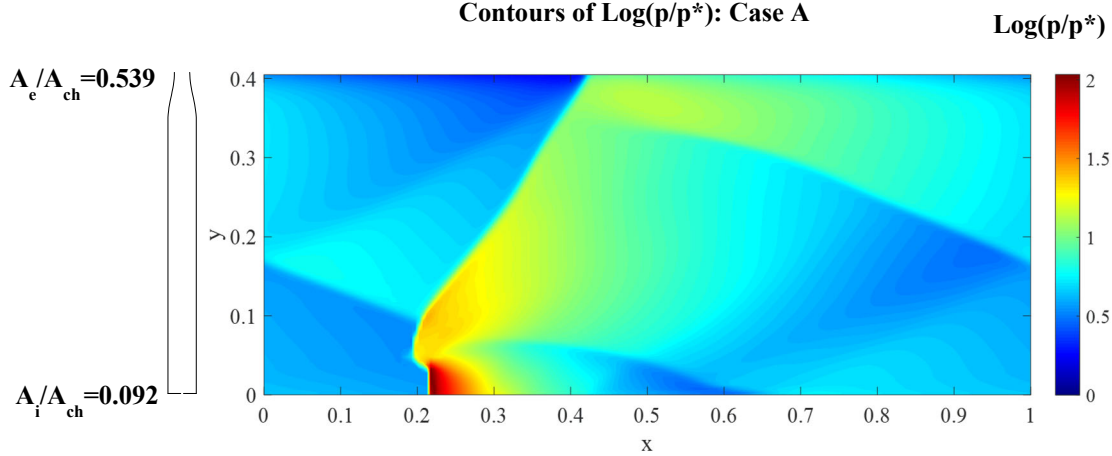
Contours of Log(p/p*): Case A

$A_e/A_{ch}=0.539$

$A_i/A_{ch}=0.092$

Fig. 5 Simulated pressure inside the RDC annulus for Case A. (Note: p*=reference pressure, 56.3 kPa)

Note, there is an area of locally high pressure (in yellow) after the shock reflects at the nozzle exit. The shock reflections are present throughout the flow field in a diamond pattern and demonstrate the complex nature of a time-resolved spatial pressure profile within the RDC annulus.

The time-averaged pressure profile in Fig. 4b can be thought of as the average pressure along a slice at a specific y-axis value of Fig. 5. This provides a visual basis for the discussion of Fig. 4b, particularly when viewing the region just downstream of the detonation zone. Figure 5 makes it clear that while a shock is still present along the axial slice, $y=0.05$ (corresponding to $z=15$ mm in Fig. 4b), the pressure would average to a lower value than that at a slice through the detonation region. The lower pressure in the reflected shock interacts with the expansion region behind the oblique shock and detonation waves at $0.3< x <0.6$. While not further explored in this study, these effects of reflected shocks seem to decrease the average pressure at $z=15$ mm in Fig 4b. While the time-averaged static pressure profile omits details of the immense fluctuations associated with the detonation and various shock reflections, it is useful when seeking effects of unique features of the flow. These features can be difficult to perceive with a spatial pressure contour plot from computations or certainly limited point measurements from experiments.

Case A: Velocity Profile Comparison

Velocity measurements 1 mm downstream of the nozzle throat and computed velocity at the nozzle throat are compared in Fig. 6. The radial location of the measurements is the throat midpoint. Measurements in Fig. 6a show 2.5 consecutive cycles of time-resolved axial velocity data from PIV. Cycle time (peak-to-peak, specifically after a minimum trough) is between 150 μs to 160 μs, corresponding to the 6.4 kHz (156 μs) wave frequency. The first cycle of measured axial velocity shows a peak of 1,400 m/s at times 50 μs and 130 μs. The disparity in peak velocity values from cycle to cycle indicates that the cycle time is not a precise multiple of the PIV sampling rate, i.e., the peak velocity in the cycle may occur sometime after the wave passage during the 10 μs time window from image to image. Thus, some disparity in the maximum velocity is expected from cycle-to-cycle. Moreover, cycle-to-cycle variations in the flow field can be expected owing to the turbulent mixing effects. The second cycle follows an expected axial velocity cyclic trend. The difference between these two cycles highlights the necessity for tools to cyclically ensemble average PIV velocity data, increasing the effective temporal resolution of velocity measurements.

The computed axial velocity profile in Fig 6a is shown for 2.5 consecutive cycles by repeating simulation results for a single cycle. Axial velocity results for both simulation and experiment compare reasonably well despite the challenges of conducting PIV in an RDC environment. The velocity spikes from a passing shock are similar in location and amplitude. However, the computed axial velocity is absent of the low velocity troughs just preceding the spikes that are present in the measured data. While axial velocity shows good agreement, the circumferential velocity, shown in Fig. 6b, tends to be overpredicted in the simulation compared to the measurements by nearly a factor of two. While the troughs show good agreement in this instance, the best way to compare this data is with an ensemble phase averaged velocity profile. Radial component of the flow field is not considered in the quasi-2D simulation and could be a source of the overprediction. Time-resolved velocity measurements tend to show a lag time on some cycles as the wave passes. The first cycle in Fig. 6b shows a 50 μs region where the flow direction changes compared to a near instantaneous flow direction change seen from the simulation. This disparity improves as the second wave passes to
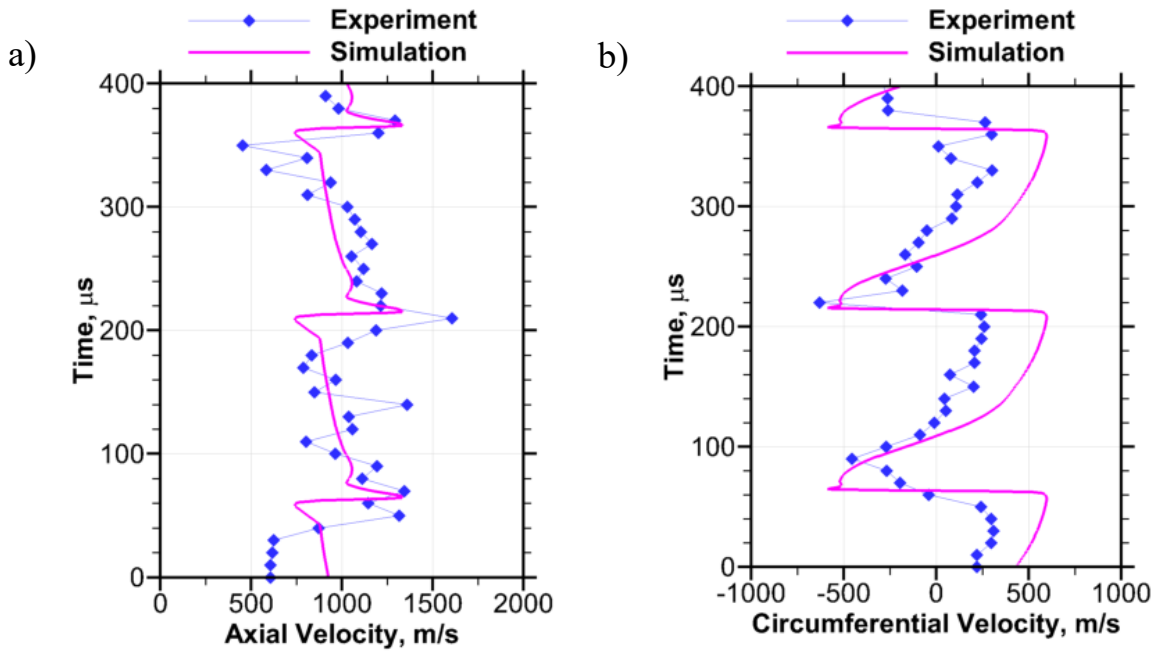
Fig. 6 Comparison of simulated and measured (a) axial velocity and (b) circumferential velocity at the annulus exit for Case A.

10 μs but tends to become slow again into the third passing of the wave. Since the PIV images are limited to 10 μs between resolved image pairs, the response rate of 10 μs at the direction change near, t=210 μs, is the best shock capture resolution the measurement has in this study.

Case B: Dynamic & Static Pressure Comparison

Case B operates at 60% of the mass flowrate of Case A. Figure 7 shows the experimental time-history of pressure in the fuel and oxidizer manifolds upstream of the injection point for Case B. The fuel manifold pressure is steady at around 600 kPa, while the oxidizer manifold average pressure is 680 kPa. As expected for a chocked flow through the injection nozzles, these manifold pressures are about 60% of the steady manifold pressures measure for Case A.

Figure 8 shows the dynamic pressure data for Case B. Experimental values are again shown for 3 consecutive cycles and reveal a phase-locked double peak behavior similarly to Case A. While Case B has a lower flowrate than
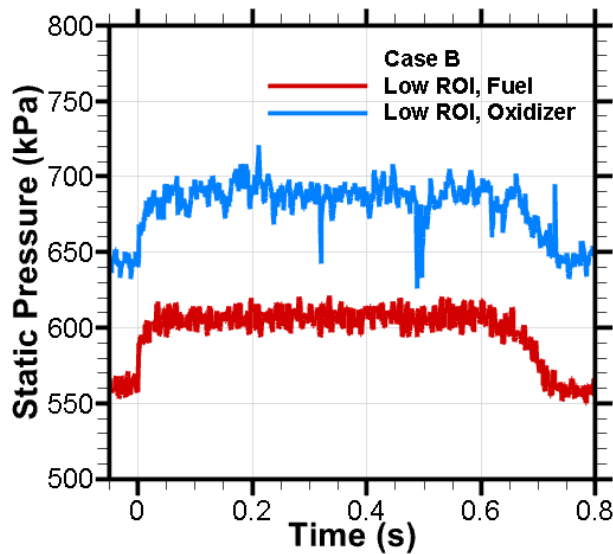

Fig. 7 Case B (low flowrate) fuel and oxidizer manifold pressure history from experiment
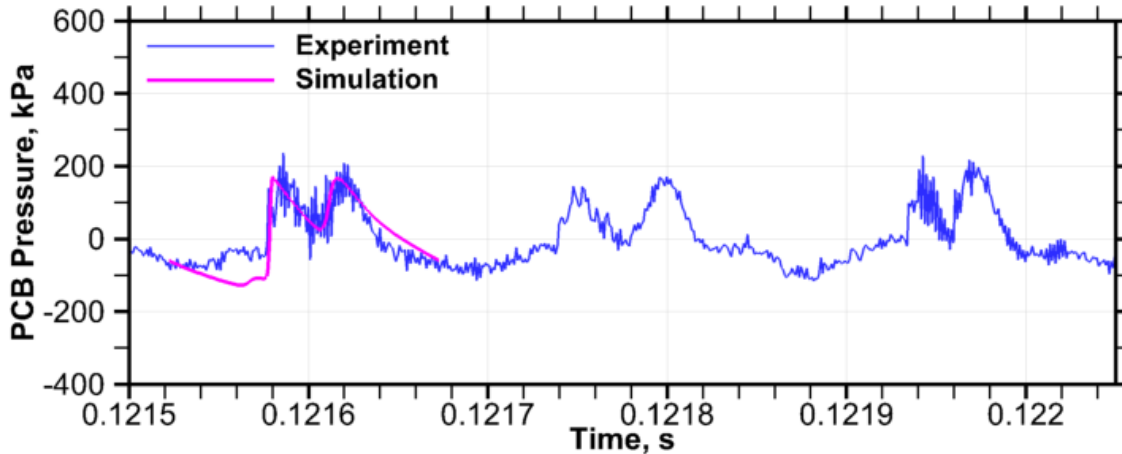
8

Fig. 8 Comparison of measured and simulated dynamic pressure inside the RDC annulus $z = 92.0$ mm for Case B.

Case A, the behavior of reacting flow still produces a shock reflection at the nozzle which travels back through the combustion products within the annulus. The experimental measurements show that the double-peak amplitudes are nearly equal for each cycle. Simulated dynamic pressure profile shows a good agreement with Case B experimental results. The shock front and reflection are both visible as the peak dynamic pressures are equal within the simulated steady cycle. The peak-to-peak time between the computed and measured data again predicts a 6.6 kHz operation for the simulation, while the measurement shows 6.0 kHz wave frequency. While several causes may bring about this disparity, the most likely reason is that the lower injection pressure from the fuel and oxidizer manifolds in Case B does not promote fuel-oxidizer mixing as well as Case A and thus effects of less consistent wave speed and in this case, slightly decreased wave speed is observed. Overall, the comparison of measured and simulated dynamic pressure agree reasonably well.

Fig. 9a presents static pressure measurements for Case B. CTAP 1 at z=22.3 mm shows an average pressure of 275 kPa and CTAP 3 at z=92 mm shows an average pressure of 255 kPa. Both manifold pressures reach steady state 50 ms after ignition. Fig. 9b compares the simulated time-averaged static pressure along the annulus with the steady-state CTAP 1 and CTAP 3 measurements. The calculated pressure of 255 kPa at the CTAP 1 location is within 7.5% of the measured steady-state pressure of 275 kPa. The computed and measured pressures at the CTAP 3 location match and both are 250 kPa. Again, the computed time-averaged static pressure is in good agreement with the measured CTAP values. Case B simulations show the non-linear profile shape of the time-averaged static pressure similarly to Case A. Thus, the computational procedure used in this study is effective at multiple reactant flow rates.

Case B: Velocity Profile Comparison

Velocity measurements at, z=1 mm, downstream of the nozzle throat and computed velocity at the nozzle throat are compared in Fig. 10. The measurements and repeated single-cycle simulation for the axial component in Fig. 10a show a reasonable agreement. The first experimental cycle data is nearly identical with the second cycle showing a lower axial velocity after the passing shock but agreeing well later in the cycle before the next shock arrival. The computed profile shows a sharp increase at the passing shock followed by a slight decrease in velocity, however the velocity stays high near 1000 m/s dropping gradually to 800 m/s, and then decreases significantly to 300 m/s before the shock again passes. The likely reason is that the flow in the exit plane for the Case B simulation is not choked over most of the low velocity region.

The circumferential velocity, shown in Fig. 10b, again tends to be overpredicted in the simulation compared to the velocity measurements by nearly a factor of two. Since radial component of the flow field is not considered in the quasi-2D simulation, this could be a source of the overprediction. The measured circumferential velocities are nearly identical in range for both cases from -250 m/s to +250 m/s. The simulated circumferential velocity is identical in profile shape between the two cases with both peaks at +600 m/s and troughs of -500 m/s for Case A and -400 m/s for Case B. Overall, the velocity comparison of measured versus simulated results for Case B is similar to the findings from Case A. This yields confidence in both the experimental and numerical approach used as an initial comparison to describe the flow physics near the exit of the RDC although more accurate representation of nozzle throat geometry might be necessary to resolve the disparity.
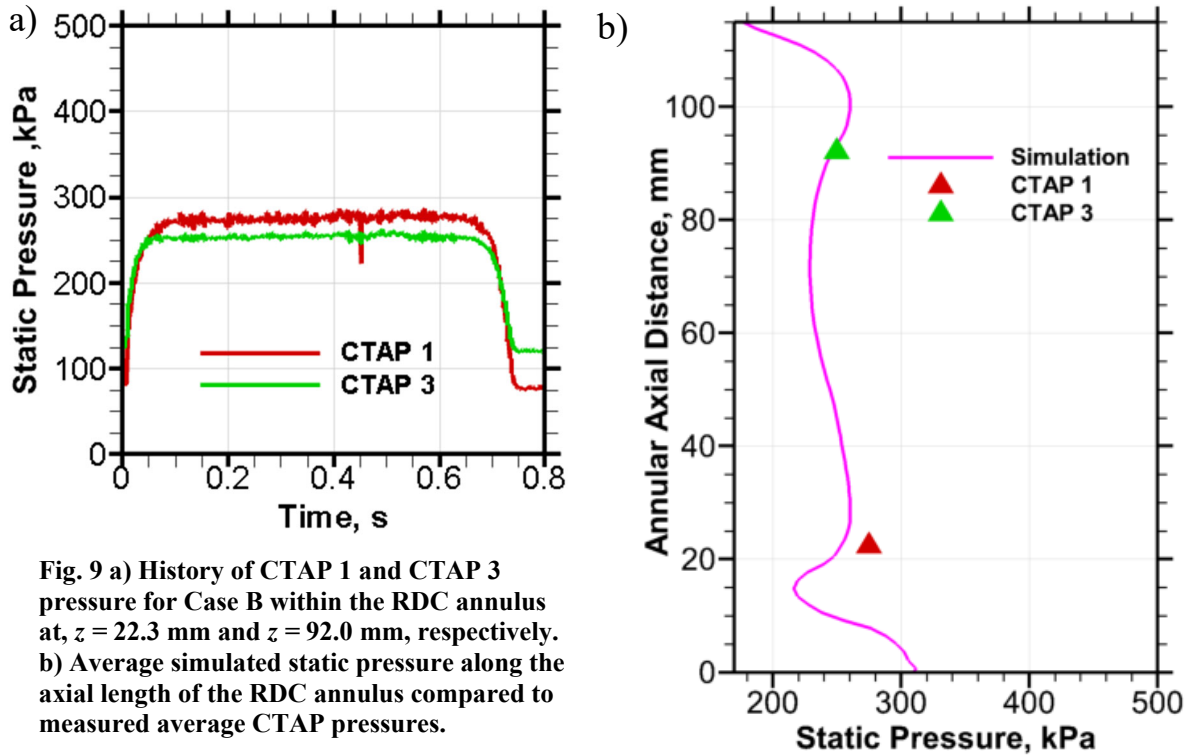
9

Fig. 9 a) History of CTAP 1 and CTAP 3 pressure for Case B within the RDC annulus at, $z = 22.3$ mm and $z = 92.0$ mm, respectively. b) Average simulated static pressure along the axial length of the RDC annulus compared to measured average CTAP pressures.

All of the generally favorable comparisons presented between experiment and code are sensitive to the predicted heat transfer to the walls of the RDC at nearly the room temperature. This amounts to approximately 22% of the available chemical energy. While this calculated heat loss cannot be validated with this experiment, it is noted that comparisons made with the assumption of adiabatic operation are poor in terms of pressures, mass flow rates, and velocities.

VI.   Conclusions

Flow field characterization is paramount for successful integration of the RDC with the rest of the system. Simulations are a useful research tool for RDC analysis but require validation with experimental results. By combining pressure measurements from inside an RDC and flow measurements at the nozzle throat of the RDC, simulations can be validated across multiple computational parameters. This study presents such an effort to reach the following conclusions:

The peak-to-peak time between the measured and computed dynamic pressure data show reasonable agreement with the CFD code predicting RDC single-wave operation at 6.6 kHz operation for both flow cases, while the measurements show wave frequency of 6.4 kHz – about 80% C-J speed for Case A (high flow rate), and 6.0 kHz Case B (low flow rate). Strong agreement in the intra-cycle behavior of dynamic pressure from measurements and computations was demonstrated.

- Computed static pressures agree well with the measured CTAP 1 location with values differing by only 6% for Case A and 7.5% for Case B and matching CTAP 3 values for both the simulation and experiment in each case. This agreement in time averaged pressure offers confidence to the accuracy of the simulations.
- The profile shape of the time-averaged static pressure from the simulation takes on a significant non-linear shape from the RDC injection location to the nozzle throat exit. The time-averaged static pressure profile is useful when seeking unique features of the flow.
- Despite the challenges of conducting PIV in an RDC environment, axial velocity results for both simulation and instantaneous experimental velocity compare reasonably well in each case. The axial velocity spikes from a passing shock are similar in location and amplitude although the troughs from the measurements are generally less than the computed velocity. The low flow rate Case B also shows a slightly different shaped axial velocity profile since the flow field is not fully choked throughout the cycle at the nozzle throat.
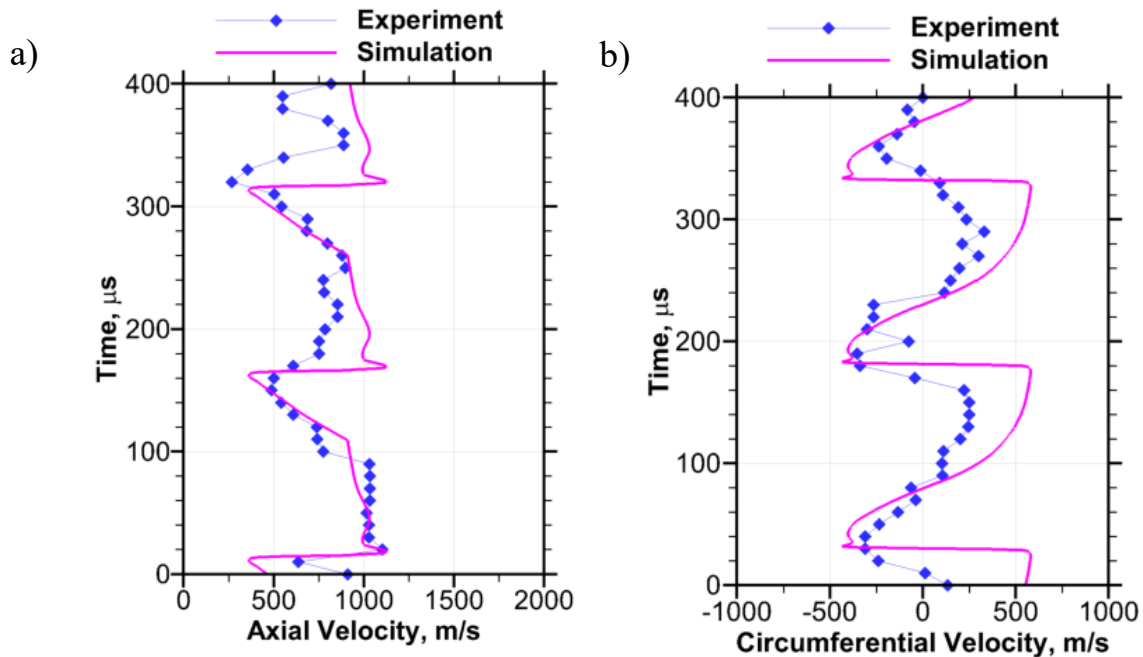
Fig. 10 Case B comparison of simulated and measured (a) axial velocity and (b) circumferential velocity at the annulus exit

Overall, the results from the experiment and simulation show good agreement. This gives confidence in the fidelity of the PIV measurements and the simulations. Future work would include 3D simulation of the RDC such that the radial component of the flow velocity can be compared to experimental measurements.

Acknowledgments

References

[1]   Zel'dovich, Yakov Borisovich. "Energy utilization of detonation combustion." Zh. Tekh. Fiz., Vol. 10, No. 17, (1940): pp. 1455—1461.

[2]   Frolov, Sergey M., Aksenova, Victor, Guseva, P. A., Ivanova, Vladislav, Medvedeva, S.N., and Shamshina, Igor. "Experimental Proof of the Energy Efficiency of the Zel'dovich Thermodynamic Cycle." Physical Chemistry Vol. 459 Part 2 (2014): pp. 207-211.

[3]   Frolov, Sergey M., Aksenova, Victor, Ivanova, Vladislav. "Experimental proof of Zel'dovich cycle efficiency gain over cycle with constant pressure combustion for hydrogen-oxygen fuel mixture", International Journal of Hydrogen Energy Vol. 40 (2015): pp. 6970-6975.

[4]   Sousa, Jorge, Paniagua, Guillermo, and Morata, Elena Collado. "Thermodynamic analysis of a gas turbine engine with a rotating detonation combustor." Applied Energy Vol. 195 (2017): pp. 247-256.

[5]   Voitsekhovskii, Bogdan Vyacheslavovich. "Stationary spin detonation," Soviet Journal of Applied Mechanics and Technical Physics No. 3 (1960) pp. 157-164.

[6]   Nicholls, J. A., and Cullen, R. E. "The Feasibility of a Rotating Detonation Wave Rocket Motor," Univ. of Michigan, TR-RPL-TDR- 64-113, Ann Arbor, MI, 1964.

[7]   Lu, Frank K. and Braun, Eric M., "Rotating Detonation Wave Propulsion: Experimental Challenges, Modeling, and Engine Concepts." Journal of Propulsion and Power Vol. 30, No. 5 (2014) p. 1125-1142.

[8]   Wolanski, Piotr, "Detonative Propulsion." Proceedings of the Combustion Institute, Vol. 34, Issue 1 (2013): pp. 125-158.

[9]   Bykovski, F.A. and Zhdan, S.A., "Current Status of Research of Continuous Detonation in Fuel–Air Mixtures (Review)." Combustion, Explosion and Shock Waves Vol. 51, no.1 (2015) pp.21-35.

[10] Kailasanath, Kazhikathra. "Recent Developments in the Research on Rotating-Detonation-Wave Engines." 55th AIAA Aerospace Sciences Meeting, AIAA 2017-07849-13, Grapevine, Texas, January 2017.

[11] Rankin Brent A., Richardson Daniel R., Caswell Andrew W., Naples Andrew G., Hoke John L., Schauer Frederick R. "Chemiluminescence imaging of an optically accessible non-premixed rotating detonation engine", Combustion and Flame Vol. 176. (2016) 12-22.

[12] Tobias, J., Depperschmidt, D., Miller, R., Uddi, Mruthunjaya, and Agrawal, Ajay K. "OH* Chemiluminescence Imaging of the Combustion Products from a Methane-Fueled Rotating Detonation Engine." Journal of Engineering for Gas Turbines and Power, Vol. 141, Issue 2 (2019).

[13] R. Miller, J. Tobias, K. Bell, D. Langner, A.K. Agrawal. "Rainbow Schlieren Imaging of Density Field in the Exhaust Flow of Rotating Detonation Combustion", AIAA Propulsion and Energy Forum. AIAA 2019-4379. 19-22 August 2019, Indianapolis, IN. https://doi.org/10.2514/6.2019-4380

[14] Paxson, D.E., Hoke, J.L., "Time Averaged Pressure Measurement in Fundamentally Unsteady Pressure Gain Combustion Systems," in Proc. JANNAF 45th Combustion Subcommittee, 33rd Airbreathing Propulsion Subcommittee, 27th Propulsion Systems Hazards Subcommittee, Monterey, CA, December, 2012, also NASA/TM—2013-217826, January, 2013.

[15] Welch, Cooper, Depperschmidt, Daniel, Miller, Robert, Tobias, Jonathan, Uddi, Mruthunjaya, and Agrawal, Ajay K. "Experimental Analysis of Wave Propagation in Methane-Fueled Rotating Detonation Combustor," Proceedings of ASME Turbo Expo 2018, ASME Paper GT2018-77258, Oslo, Norway, June 11-15, 2018.

[16] Depperschmidt, D., Tobias, J., Miller, R., Uddi., M., Agrawal, A.K., Stout, J.B., Time-Resolved PIV Diagnostics to Measure Flow Field Exiting Methane-Fueled Rotating Detonation Combustor, AIAA-2019-1514, Presented at AIAA SciTech Forum 2019, San Diego, California, January 7-11, 2019.

[17] Rankin, B.A., Fotia, M.L., Paxson, D.E., Hoke, J.L., Schauer, F.R., "Experimental and Numerical Evaluation of Pressure Gain Combustion in a Rotating Detonation Engine," AIAA-2015-0877, January 2015.

[18] Theuerkauf, S.W., et al, "Comparison of Simulated and Measured Instantaneous Heat Flux in a Rotating Detonation Engine," AIAA-2016-1200, January 2016.

[19] Paxson, D.E., Fotia, M.L., Hoke, J.L., Schauer, F.R., "Comparison of Numerically Simulated and Experimentally Measured Performance of a Rotating Detonation Engine," AIAA-2015-1101, January 2015.

[20] Paxson, D.E., "Numerical Analysis of a Rotating Detonation Engine in the Relative Reference Frame," AIAA-2014-0284, January 2014, also NASA/TM 2014-216634, 2014.

[21] Perkins, H.D., et. al., "An Assessment of Pulse Detonation Engine Performance Estimation Methods Based on Experimental Results," AIAA 2005-3831, July 2005.

[22] Paxson, D.E., Naples, A.G., Hoke, J.L., Schauer, F. "Numerical Analysis of a Pulse Detonation Cross Flow Heat Load Experiment," AIAA-2011-584, January 2011.

[23] Paxson, D.E., Schauer, F.R., Hopper, D., "Performance Impact of Deflagration to Detonation Transition Enhancing Obstacles," AIAA-2009-0502, July 2009, also, NASA/TM—2012-217629.

[24] Paxson, D.E., "A General Numerical Model for Wave Rotor Analysis," NASA TM 105740, 1992.

[25] Paxson, D.E., "An Improved Numerical Model for Wave Rotor Design and Analysis," AIAA-93-0482, January 1993.